**ORIGINAL ARTICLE**

# Quantitative Determination of 3D-Printing and Surface-Treatment Conditions for Direct-Printed Microfluidic Devices

Hyun Namgung[1] · Abdi Mirgissa Kaba[1] · Hyeonkyu Oh[1] · Hyunjin Jeon[1] · Jeonghwan Yoon[1] · Haseul Lee[1] · Dohyun Kim[1]

## Abstract

We report a quantitative and systematic method for determining 3D-printing and surface-treatment conditions that can help improve the optical quality of direct-printed microfluidic devices. Digital light processing (DLP)-stereolithography (SLA) printing was extensively studied in microfluidics owing to the rapid, one-step, cleanroom-free, maskless, and high-definition microfabrication of 3D-microfluidic devices. However, optical imaging or detection for bioassays in DLP-SLA-printed microfluidic devices are limited by the translucence of photopolymerized resins. Various approaches, including mechanical abrasions, chemical etching, polymer coatings, and printing on transparent glass/plastic slides, were proposed to address this limitation. However, the effects of these methods have not been analyzed quantitatively or systematically. For the first time, we propose quantitative and methodological determination of 3D-printing and surface-treatment conditions, based on optical-resolution analysis using USAF 1951 resolution test targets and a fluorescence microbead slide through 3D-printed coverslip chips. The key printing parameters (resin type, build orientation, layer thickness, and layer offset) and surface-treatment parameters (grit number for sanding, polishing time with alumina slurry, and type of refractive-index-matching coatings) were determined in a step-wise manner. As a result, we achieved marked improvements in resolution (from 80.6 to 645.1 lp/mm) and contrast (from 3.30 to 27.63% for 645.1 lp/mm resolution). Furthermore, images of the fluorescence microbeads were qualitatively analyzed to evaluate the proposed 3D-printing and surface-treatment approach for fluorescence imaging applications. Finally, the proposed method was validated by fabricating an acoustic micromixer chip and fluorescently visualizing cavitation microstreaming that emanated from an oscillating bubble captured inside the chip. We expect that our approach for enhancing optical quality will be widely used in the rapid manufacturing of 3D-microfluidic chips for optical assays.

**Keywords** DLP-SLA 3D printing · Microfluidic chip · Microfabrication · Optical resolution · Surface treatment

## 1 Introduction

Three-dimensional (3D) printing was first developed in the early 1980s in the form of stereolithography (SLA) [1–10]. 3D printing allows the assembly-free, high-definition manufacturing of a freeform, semi-arbitrary 3D object directly from a CAD design [6, 7, 11, 12]. Furthermore, material consumption can be reduced, in contrast to subtractive manufacturing, such as machining or laser ablation [6, 7, 11]. Since its inception, several 3D-printing methods, including fused deposition modeling (FDM), selective laser sintering (SLS), laminated object manufacturing (LOM), and multi-jet modeling (MJM), have been developed [3, 7, 8, 11, 13]. 3D-printing has the potential to revolutionize manufacturing in various industrial fields by (1) prototyping products and parts rapidly (e.g., automotive, aerospace, and defense industries), which can facilitate overall research and development processes; and (2) customizing a product for the requirements of an individual user (e.g., prosthetics, implants, and shoes) [1, 7, 8, 14].

Many microfluidic devices have been fabricated using polydimethylsiloxane (PDMS)-based soft lithography for

Hyun Namgung and Abdi Mirgissa Kaba have contributed equally to this work.

✉ Dohyun Kim
dohyun.kim@mju.ac.kr

1 Department of Mechanical Engineering, Myongji University, 116 Myongji-ro, Yongin 17058, Republic of Korea

more than the past 20 years. Soft lithography has advantages over conventional cleanroom-based microfabrication techniques established in the MEMS and microelectronics industries: low cost, biocompatibility, optical transparency, gas-permeability (i.e., cell culture), mechanical elasticity (i.e., Quake's valve), cleanroom-free fabrication, and relatively short user training [8, 13, 15]. However, soft lithography has critical limitations when translated into mass manufacturing [2, 8]. Soft lithography is largely a slow and manual process that requires molding, demolding, alignment, and bonding of multiple PDMS layers. Therefore, it is challenging to scale up the manufacturing process [12, 15]. Furthermore, the properties of PDMS are vastly different from those of hard plastics, including polymethyl methacrylate (PMMA), polystyrene (PS), and polycarbonate (PC), which are routinely used in mass-produced microfluidic devices [2]. Moreover, a master mold for soft lithography is typically fabricated using SU-8 photolithography, which is still limited by conventional cleanroom-based microfabrication [5, 15, 16]. Even by stacking multiple layers, a PDMS microfluidic device remains 2.5D, unable to take advantage of a genuine 3D design [2, 8, 11]. Lastly, interfacing with a PDMS microfluidic device (i.e., punching holes and securing metal tubes) lacks standardization, is prone to leakage, and proves labor intensive [6, 8]. Thus, only a handful of PDMS-based microfluidic products are currently sold in the market (e.g., Fluidigm) [8, 17].

3D printing has been rapidly adopted by the microfluidics community, addressing the limitations of soft lithography [9, 10, 18, 19]. First, 3D printing can be performed without a cleanroom [5, 15], and now desktop 3D printers have become more affordable [6, 13]. This has made 3D printing accessible to many microfluidic researchers. Second, tedious manual alignment and bonding are not required because the entire device can be printed in one step [20, 21]. Third, the polymer materials used in 3D printing are more similar to those used in mass manufacturing than PDMS [2]. Therefore, the technological translation to a commercial scale is considerably easier [2, 12]. Fourth, interfacing with 3D-printed microfluidic devices is more straightforward and secure than PDMS counterparts using standardized fluidic couplings (e.g., Luer-Lock, barb types). CAD designs of those couplings can be easily downloaded (e.g., Grabcad) and embedded into a device design [3, 8, 11–13]. Finally, a truly 3D-microfluidic device can exploit the potential of freeform geometry such as intricate vertical fluidic connections, inclined structures, and spiral channels, compared to PDMS devices limited in 2.5D [2, 12]. Now entire microfluidic devices are routinely 3D-printed [12, 21]. Among the aforementioned various 3D printing methods, DLP (digital light processing)-SLA, is deemed the most suitable for microfluidics because it can realize superior printing resolution (as low as 2 μm *XY* resolution and 1 μm *Z*

resolution) [2, 22], better surface finish [14, 23], more secure device sealing [14], faster support removal (i.e., by suction of uncured resin) [6, 8], and faster printing [14, 15]. Therefore, an increasing number of microfluidic devices have been fabricated using DLP-SLA printing [16, 21, 24, 25].

DLP-SLA printing has a few limitations [2, 8, 24], including inferior resolution (compared to the soft-lithography resolution), cytotoxicity, gas impermeability, and complexity in multi-material printing. However, optical transparency is one of the critical limitations that has not been thoroughly addressed [5, 8, 11]. The transparency of a microfluidic device is essential because optical observation and detection (e.g., fluorescence and UV–Vis absorbance) are routinely performed [26–28]. The surface roughness and bulk volume defects of a printed structure were reported to reduce transparency because of light diffraction and scattering [28, 29]. Various origins of surface roughness have been suggested, including (1) photopolymerization on the textured (anodized) surface of a build platform [26, 28]; (2) photopolymerization on a polymer-film window of a vat bottom, which is scratched by continuous delamination with a metal slider [28]; and (3) the pixelation of a polymerized surface [30, 31] because of a grid-like illumination pattern from millions of micromirrors in a DLP chip [32, 33].

Several approaches have been employed to improve surface roughness [7, 20, 28], including (1) mechanical abrasive treatment such as sanding [26, 34, 35] and diamond polishing [35, 36]; (2) chemical treatment such as solvent-fume polishing [37]; (3) polymer coatings [38] such as PDMS [39], epoxy [40], and acrylic spray [41]; (4) refractive-index (RI) matching using oils [25, 42, 43]; and (5) printing on pristine glass or plastic plates [44]. However, these methods lacked quantitative and systematic assessment of the optical-quality improvement using metrics such as resolution and contrast. In most cases, the optical-quality improvement was qualitatively validated by imaging cells [25, 26] or microstructures [25].

In this work, we aim to address this limitation by taking a novel approach based on a USAF 1951 optical-resolution test chart. It consists of several test patterns, three horizontal and three vertical lines with progressively smaller widths and spacings [45]. The line widths and spacings span from 2 mm (group −2 and element 1) to 0.55 μm (group 9 and element 3), which can be translated into a resolution of 0.250 lp/mm (line pair per mm) to 912.3 lp/mm, respectively. Resolution is measured by the smallest test patterns, of which all lines are optically distinguished by an observer. The USAF 1951 test chart is widely used in optics and optical engineering to quantify the performance of optical systems such as lenses, image sensors, and projection systems [46–49].

To the best of our knowledge, this is the first study to use USAF 1951 charts to quantitatively and systematically analyze the improvement in the optical quality of

DLP-SLA-printed microdevices for the purpose of optimizing 3D-priting and surface-treatment conditions. We "semi-optimized" 3D-printing and surface-treatment conditions via the *step-wise* modification of a single parameter in a seven-dimensional parameter space so that a printed microfluidic device could yield the best resolution through an optical window at the top. To prove the concept, we selected important build parameters, (1) resin type, (2) printing orientation, (3) layer thickness, and (4) layer offset, and determined parameter values that yielded the best resolution. Then, we established surface-treatment conditions in a similar manner. We opted to determine the conditions for the key surface-treatment methods: (5) sanding, (6) alumina polishing, and (7) RI matching. These methods are relatively straightforward and safe compared to techniques such as solvent-fume etching and acrylic spray. Finally, we validated our quantitative, systematic, and experimental approaches to optical-quality improvement by printing operational test microfluidic devices. We demonstrated a 3D-printed micromixer chip based on cavitation microstreaming. The streamlines generated by an oscillating bubble in the micromixer chips that were prepared using unoptimized and optimized conditions were visualized, and the corresponding streamline images were compared in terms of optical quality.

## 2 Materials and Methods

### 2.1 Materials

Three popular, commercial, clear resins for stereolithography (SLA) printing were employed for comparison: PlasCLEAR of Asiga (Alexandria, Australia), PR48 (open-source resin developed by Autodesk, manufactured by CPS, Boulder, Colorado, United States), and GR-10 from Pro3dure Medical (Iserlohn, Germany). 99.95% isopropanol for washing cover chips was purchased from Duksan Pure Chemicals (Ansan, South Korea). Sandpaper disc pads of 1000, 2000, 3000, and 5000 grits were obtained from Jiangsu Dongyan Abrasive Tools (Jiangsu, China). Polishing cloth pads were purchased from PartLine (Anyang, South Korea) and used with a 50-nm alumina slurry (product code: #17727101999) from Metallurgical Supplies (Tonawanda, New York, United States). Sandalwood oil (RI $n = 1.5–1.51$) was purchased from Herbnoori (Daegu, South Korea), and AP 150 Wacker silicone oil ($n = 1.51$, #330779) was obtained from Sigma (St. Louis, Missouri, United States). Fluorescence microbeads (emission wavelength $= 485$ nm, #FH-10052-2) for flow-field visualization were purchased from Spherotech (Lake Forest, Illinois, United States).

Two USAF 1951 resolution test targets were used for the quantitative optical-quality analysis of printed chips. A low-resolution chart (from group 2—element 1 to group 7—element 6, #R3L1S4P) was obtained from Thorlabs (Newton, New Jersey, United States), and a high-resolution chart (from group 2—element 1 to group 9—element 3, #PS75P) was from Graticules Optics (Tonbridge, United Kingdom). A microscope calibration slide with embedded fluorescence beads (StarLight, #25442-1) from Polysciences (Warrington, Pennsylvania, United States) was used to qualitatively assess 3D-printing and surface-treatment conditions and to evaluate the proposed post-fabrication process for fluorescence imaging applications.

### 2.2 Slide-Cover Chip Fabrication and Imaging-Based Determination of Optical Quality

A slide-cover chip was fabricated using various 3D-printing and surface-treatment conditions. The cover chip has a bracket "[" shape that fits properly to resolution test targets of the standard glass-slide format (75 mm × 25 mm) as shown in Fig. 1. The top-plate thickness of the chip was designed as 400 µm (build-plate thickness of 50 µm was added to the final thickness during printing), and the thickness of the arms was designed as 1 mm (Fig. 1a). The top plate should be as thin as possible for better light transmission; however, 400 µm was selected because the thinner top
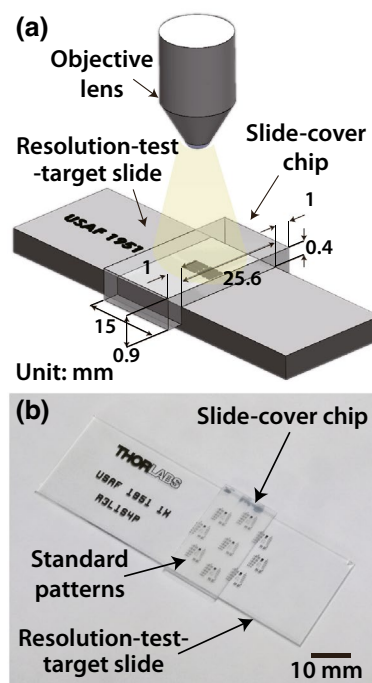


**Fig. 1** Slide-cover chip and USAF 1951 resolution target. **a** Schematic of slide-cover chip, properly fit on the resolution target. Bright-field and fluorescence images of the target were captured via the top plate of the chip, using an upright microscope equipped with an sCMOS camera. The dimension was given in millimeters. **b** The photograph of the cover chip fitted on the resolution target

plates tend to bend after printing. The chip was rinsed twice using isopropanol in a sonicated bath with an ultrasonic cleaner UC-20, purchased from Jeiotech (Daejeon, South Korea) for a total of 15 min. Then the chip was exposed to UV light for 10 min to complete photopolymerization in a compact UV oven (Asiga Flash). The completed cover chip was tightly fitted to the resolution target, as indicated in Fig. 1b.

The optical quality of each cover chip was analyzed by optical resolution, which was determined by the visual inspection of brightfield images. These images were captured using an upright microscope (BX40) from Olympus (Tokyo, Japan), equipped with an sCMOS camera (#CS2100M-USB) from Thorlabs. The low-resolution target (Fig. 2a) contains standard patterns from groups 2 to 7 (equivalent to the resolution of 4.00–228.1 lp/mm). The images of the low-resolution test target were captured with a 10× objective lens (UPlanFL, Olympus). The resolution was practically identical (indistinguishable test patterns) throughout the sanding step (Sect. 2.4), even with progressively refined sanding conditions. Therefore, higher resolution patterns from groups 8 to 9 in the target from Graticule Optics (Fig. 2b) were used for the sanding and subsequent steps. Their images were taken with a 40× objective lens (UPLanFL, Olympus).

We considered a pattern resolved if all three vertical and horizontal lines were distinguished by the Rayleigh criterion [45]. First, a grayscale image of a specific pattern was inverted (i.e., black rectangles turned white ones). The resulting pixel intensity was measured using ImageJ, developed by the National Institutes of Health (Bethesda, Maryland, United States). Second, we considered a specific

pattern optically resolved when the intensity value for each trough (black rectangular gap between two white rectangular features) was above 74% of the maximum intensity among the three peaks (both vertical and horizontal). We took the average intensity of empty areas near the vertical patterns as the minimum intensity (e.g., left side of pattern group 9 and element 3 in Fig. 2b) because it was difficult to find a suitable, empty area near the horizontal patterns.

When the resolution was indistinguishable even with the high-resolution target (Graticules Optics), we resorted to the contrast values instead of using even higher-resolution charts (e.g., 2015a USAF from Ready Optics). This is because of the challenges in using high-magnification objective lenses such as short working distances and stage vibration. The intensity value $I$ of the pattern images captured under the same lighting and capture conditions, i.e., 50% power of an LED light source PE-300 Ultra (CoolLED, Andover, United Kingdom), an exposure time of 30 ms, $1 \times 1$ binning, and $1 \times$ amplifier gain, was measured using ImageJ. Then, the contrast (%) was calculated as:

$$\text{Contrast}(\%) = \frac{I_{\max} - I_{\min}}{I_{\max} + I_{\min}} \times 100(\%). \tag{1}$$

We calculated the average of contrast values from two rectangular pairs (horizontal and vertical) and considered a pattern to be in higher contrast if both average values were larger.

The fluorescence images of microbeads in the calibration slide were also captured. We used an upright epi-fluorescence microscope BX50 (Olympus), equipped with a Peltier-cooled CCD camera CoolSNAP HQ$^2$ (Photometrics, Tucson, Arizona, United States), and the same 10× and 40× objective lenses and a fluorescence filter set (U-MWB, Olympus). The fluorescence images aided in determining the optical quality of the cover chips when the two brightfield images were indiscernible. As the resolution was chiefly analyzed using brightfield images, fluorescence images were used to confirm if high-quality fluorescence imaging could be performed through microfluidic chips printed using the determined conditions.



**Fig. 2** Two USAF 1951 resolution test targets were used in this work. **a** The lower resolution target was from Thorlabs. Resolution patterns from groups 6 to 7 (inset figure) were captured using a 10× objective lens and used to evaluate the resolution until the sanding step (Sect. 2.4). **b** The higher resolution target from Graticules Optics. Resolution patterns from groups 8 to 9 (inset figure) were captured using a 40× objective lens and used to evaluate the resolution for the sanding and subsequent steps

### 2.3 Step-Wise Determination of 3D-Printing Conditions

We used PICO2 HD, a DLP-SLA printer with a UV light source (385 nm) from Asiga. It features a nominal *XY* resolution of 27 μm and a *Z* resolution of 1 μm. The PICO2 HD printer has been frequently used for microfluidic chips because of its high printing resolution [34, 50–54]. In this study, three clear commercial resins, PlasCLEAR (Asiga), GR-10 (Pro3dure), and PR48 (Autodesk), were tested. Printing parameters for PlasCLEAR were built in the printing
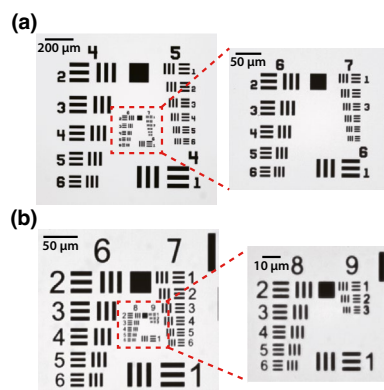
software Composer (Asiga). Although GR-10 is not an Asiga product, the company provided a material definition file (.ini file) and a basic guideline for parameter adjustment. PR48 is an open-source resin designed by Autodesk, but we were unable to obtain a material definition file. Therefore, we chose to use the same .ini file for GR-10 since the file worked with minor parameter modifications. Among the various build parameters, some basic parameters were fixed, but the rest were modified to determine a condition for improved optical quality.

For the fixed parameters, the light intensity was set at 30 mW/cm$^2$ for all resins. Exposure time, which defines the duration of UV illumination [55], was set as the default value for each resin: 6.30 s for PlasCLEAR and 0.305 s for GR-10. The exposure time for a proprietary PR48 was determined as 2.0 s, which is a slight increase from the suggested value in the literature [56]. We also determined "burn-in" exposure time. It is required to form a build plate (or "burn-in layer"), which is the first layer laminated onto the built platform. Without an appropriate burn-in layer, 3D-printed structures were often entirely delaminated from the platform or bent because of the internal stress [30, 57, 58]. The burn-in exposure time was set to 17.3 s for PlasCLEAR and 0.8 s for GR-10 as the default values. For PR48, 5.26 s was tested as a starting point because the ratio of exposure time to burn-in exposure time was 0.38 (= 2.0 s ÷ 5.26 s), which matches the exposure-to-burn-in-exposure-time ratio of PlasCLEAR and GR-10. Later, the burn-in exposure time was increased to 16 s so that the cover chips robustly adhered to the build platform. We selected the number of burn-in layers as one and the thickness of each burn-in layer as 50 μm for all resins. There can be more than one burn-in layer between the build platform and an actual structure, but we chose one to minimize an unnecessary increase in the overall chip thickness. Finally, the heater temperature was set to 25 °C.

For the remaining variable build parameters, we considered an empirical approach to determine semi-optimal values from a four-dimensional parameter space (i.e., resin type, printing orientation, layer thickness, and layer offset). In the first determination step, the first parameter (i.e., resin type) value that ensured the best resolution among the tested conditions was determined while the other three parameters (i.e., printing orientation, layer thickness, and layer offset) were fixed during the second step. Then, a second parameter (i.e., printing orientation) value guaranteeing the best resolution was determined in the second determination step. The first parameter (i.e., resin type) was transferred from the first step, and the remaining two parameters (i.e., layer thickness and layer offset) were fixed. This step-wise process was repeated until the final determination step. The same suits were followed for the determination of surface-treatment conditions. This optimization process may not be rigorous, implying a globally optimal parameter set can be missed [59]. However, to the best of our knowledge, this is the first demonstration of a quantitative and systematic determination of printing conditions for better optical quality using resolution test targets. The proposed approach of using resolution targets can be applied to more rigorous optimization methods such as design of experiment (DOE) [60, 61], nonlinear programming [62], or machine learning [63, 64]. The step-wise build-parameter determination process is as follows.

*Step 1* Three resins were used to print slide-cover chips: PlasCLEAR [26, 57, 65, 66], GR-10 [26, 67], and PR48 [7, 35, 57, 58]. These resins are popular acrylate- or methacrylate-based clear resins for printing microfluidic devices. Other initial build parameters were fixed: build orientation = top-up, layer thickness = 25 μm, and layer off-set = 80 μm. These parameters were adjusted in the subsequent steps. The best resin was selected based on measured resolving power through the slide-cover chips.

*Step 2* Once the resin type was determined, the build orientations (top-up and top-down) were compared. As shown in Fig. 3, the top plate of the cover chip adheres to the build platform during printing for the top-up orientation. Conversely, the top plate adheres to the FEP vat window for the top-down orientation. It has been reported that printing orientation significantly affects surface quality and optical transmission [30, 32, 68, 69]. We tested
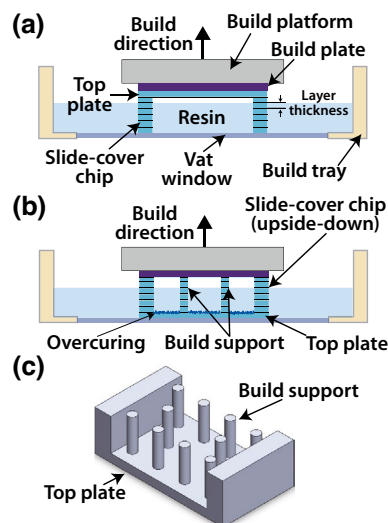


**Fig. 3** Printing orientation of a slide-cover chip. **a** Conventional top-up orientation. The top plate adheres to the textured build platform during printing, which results in a roughened surface. The build plate (i.e., burn-in layer) enhances bonding between the build platform and the structure. **b** Top-down orientation. The top adheres to the polymeric vat window during printing, which is typically scratched by a sliding metal bar. The ceiling of the top plate is affected by overcuring, which results from bleeding of UV illumination into the uncured resin above. **c** For top-down orientation, build supports are added to construct an overhanging top plate to the cover-slide chip

only the top-up and top-down orientations because it is not practical to build sideways (i.e., the top plate oriented perpendicularly to the build platform) because of a long build time. Furthermore, the angled orientation is known to generate stair-like significant surface roughness [68, 69]. For the top-up orientation, the best chip from Step 1 was evaluated because the printing conditions were identical. The top surface will be primarily affected via contact with the anodized surface of the build platform (Fig. 3a). A new inverted cover chip (Fig. 3b) is designed for top-down orientation. The design for the top-down orientation (Fig. 3c) includes build supports of a cylindrical shape (1-mm diameter). Without these supports, the top plate bent most of the time and sometimes collapsed during printing, possibly due to internal stress [30, 57, 58]. The supports and 50-μm-thick build plate were removed after the build was completed. Images were captured through the clear regions of the top plate, where the supports did not adhere. The top surface was adversely affected by scratches and blemishes on the vat window. Furthermore, it was strongly affected by overcuring under the ceiling (Fig. 3b), which significantly affected resolution because overcured surfaces contacted the test target after flipped to fit on the target (Fig. 1) [26, 31, 57, 70].

*Step 3* Layer thicknesses of 10, 25, 50, and 100 μm were tested with all the remaining printing parameters transferred from Step 2. Layer thickness is defined as the identical height of the slices generated from a solid CAD model and using slicer software (Fig. 3a). Finer slicing can approximate 3D curved surfaces more accurately but take longer to print. Considering the minimum feature size of the cover chip (> 400 μm), we selected these four thickness values for practical printing durations (7 min for 100 μm vs. 90 min for 10 μm layer thicknesses) and reasonable accuracy.

Step 4 Layer offsets of 2.5, 7.5, 12.5, and 25 μm (5%, 15%, 25%, and 50% of the layer thickness determined from Step 3, see Sect. 3) were tested with all the remaining printing parameters transferred from Step 3. Layer offset (curing-thickness offset or overcuring) is an additional amount of light exposed to the resin to prevent delamination from a previously photopolymerized slice [26, 32, 55, 57, 71]. A suitable offset is necessary for maintaining structural integrity and thus for achieving successful printing. However, an excessive offset will result in light bleeding, which will cause dimensional inaccuracy and rough surfaces in printed features. It has been noted that overly cured ceilings (or roofs) of voids are a critical problem in microfluidics because overcuring can result in a roughened surface or even clogging of narrow channels or cavities (say, < 100 μm in height) [26, 31, 57, 70]. The offset value was carefully optimized because a rough surface under the ceiling is a significant obstacle for imaging-based assays. [26, 57, 70].

## 2.4 Step-Wise Determination of Surface-Treatment Conditions

The optical quality of a planar roof of a microchannel or a microcavity is crucial, considering that optical imaging or detection is common in microfluidics applications [26–28]. It has been reported that surface roughness and bulk volume defects influence optical quality due to light diffraction and scattering [28, 29]. Various sources of rough surfaces have been reported, including: (1) polymerization on the textured anodized surface of a build platform [26, 28]; (2) polymerization on a scratched vat window (resulting from continuous delamination by a metal slider) [28]; (3) pixelation of photopolymerized surface [30, 31] due to a grid-like illumination pattern from millions of micromirrors in a DLP chip and uneven light intensity across a micromirror which acts as an aperture [32, 33]; and (4) polymerization of resins comprising different monomer/oligomer, crosslinker, photoinitiator, and photoabsorber contents [31].

Several approaches have been adopted to improve surface roughness [20, 28]: (1) mechanical abrasive treatment such as sanding [26, 34, 35] and polishing [35, 36]; (2) chemical treatments to smoothen surface blemishes such as solvent-fume polishing [37]; (3) polymer coatings [38] to cover surface defects using PDMS [39], polystyrene (PS) [39], epoxy [40], acrylic spray [41], lacquer [36], and resin followed by photopolymerization [34]; (4) RI matching using oils to hide surface roughness [25, 42, 43]; and (5) printing on an immaculate glass or plastic slide attached to the build platform to reduce the polymerization effect on a textured surface [44]. To prove the concept of our approach, we opted for mechanical treatments including sanding, alumina-slurry polishing, and RI matching, all of which are relatively straightforward and safe. Surface-treatment conditions were also determined in a similar step-wise manner.

*Step 5* We sandpapered the top surface of a cover chip fabricated using the printing parameters determined in Step 4. Each of the four sandpaper pads of 1000, 2000, 3000, and 5000 grits was attached to a potter's wheel as seen in Fig. S1a of SI (Supplementary Information) and used to grind a cover chip. DI water was added to the pad, and the chip was held for 5 min against the pad rotating at 60 rpm. The first condition was to grind with a 1000-grit pad for 5 min, and the images of the USAF 1951 target were captured through the treated chip. The second condition was to sandpaper the same chip using a 2000-grit pad for 5 min, and so forth. The sanding condition was determined by the best target resolution obtained through the treated cover chip.

*Step 6* Four slide-cover chips were printed and treated using the best conditions in Step 5. The cover chips were then polished using 50-nm alumina slurry, 2.5× diluted (w/w) with DI water, for progressively longer periods of 5, 10, 15, and 20 min. The diluted slurry solution was poured

on a polishing-cloth pad as a small puddle (~ 15 mL), and a cover chip was pushed against the pad rotating at 60 rpm for progressively longer durations (Fig. S1b in SI). After the treatment, the resolution target was imaged through all four chips, and the polishing condition was selected based on the optical resolution.

*Step 7* Cover chips prepared using the best condition in Step 6 were coated with a RI-matching film: silicone oil (RI $n = 1.51$) [42, 50], sandalwood oil ($n = 1.5–1.51$) [72], and the 3D-printing resin itself ($n = 1.5–1.52$, see Sect. 3.2 [35]). Approximately 10 μL of liquid was delivered to the cover-chip surface using a micropipette. It spread sufficiently to cover the chip surface within 1–5 min, as displayed in Fig. S1c in SI. For the resin, the chip was cured in the UV oven for 25 min for photopolymerization. Resolution-target images were captured through the coated chips. A control experiment with a chip that had no coatings (the best chip from Step 6) was also performed.

## 2.5 Design and Fabrication of a Micromixer Based on Cavitation Microstreaming

Cavitation microstreaming is a strong circulatory flow occurring around an oscillating bubble [73] and has been extensively employed for microfluidic mixing applications [74–77]. We attempt to demonstrate our approach for improving the optical quality of a 3D-printed chip by visualizing cavitation microstreaming inside a microfluidic mixer chip (Fig. 4). The micromixer chip is fabricated using 3D-printing and surface-treatment conditions established through our step-wise determination process.

The micromixer chip is an update from our previous work [74, 77]. This new design has a central mixing chamber (16-mm diameter and 201-μL internal volume) with cylindrical air pockets of 500-μm diameter and 300-μm depth for capturing bubbles at five predetermined positions (Fig. 4b). In our previous work [74, 77], the streaming coverage from bubbles was confined near the chamber perimeter. Therefore, the mixing performance was limited. In this work, air pockets were formed vertically (hung on the ceiling, inset of Fig. 4b) for better streaming coverage as long as the pocket is densely populated [78–81]. The chamber was connected to the inlet and outlet ports (2-mm diameter) through 6-mm-long microchannels. The footprint of the chip was 50 mm × 25 mm. The thickness of the chip was 2 mm, including the top plate (0.5 mm), cavity (1 mm), and bottom plate (0.5 mm). The micromixer chip was fabricated using the printing parameters established through the proposed process (Sect. 2.3). The uncured resin inside the chip was removed using a suction pump (BF-101, BioFree, Bucheon, South Korea) and dried using a nitrogen gun (Yongin Gas, Yongin, South Korea). Next, isopropanol wash and post-curing were performed. The outer surface of the top plate was
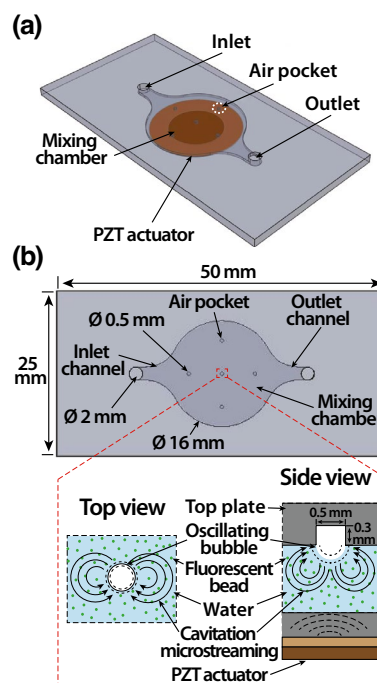


**Fig. 4** Micromixer chip based on cavitation microstreaming. **a** The mixer chip has a central chamber with five vertically arranged air pockets for trapping air bubbles. A piezoelectric (PZT) actuator is bonded to the bottom of the chip for resonance-frequency measurement and bubble excitation. **b** The dimensions of the key micromixer features are shown. Upon excitation using the PZT actuator, an oscillating bubble generates a strong circulatory flow (i.e., cavitation microstreaming) to induce mixing inside the chamber

treated using the determined surface-treatment conditions (Sect. 2.4). Finally, a lead zirconate titanate (PZT) actuator (7BB-15-6L0, Murata, Kyoto, Japan) was bonded to the bottom of the chip at the center using a superglue (Loctite 401, Henkel, Dusseldorf, Germany). The piezoelectric actuator has dual purposes: the determination of the resonance frequency and excitation of trapped air bubbles [74, 77].

## 2.6 Mixing Experiment and Streamline Generation Using the 3D-Printed Micromixer Chip

When a bubble is excited at its resonance frequency, it exhibits effective cavitation microstreaming [73]. Our group established a rapid and convenient method for determining the resonance frequency using an electromechanical impedance spectroscopy (EMIS) technique [74, 77]. The technique was also implemented for our new 3D-printed micromixer chip. Briefly, the chip was filled with DI water, and the inlet/outlet ports were sealed with Teflon tape (#AG021AD) from Alphaflon Teflon Specialist (Seoul, South Korea). The chip was then mounted in a custom jig designed to clamp the chip, as presented in Fig. 5a. The jig was printed using an FDM 3D printer (3DWOX) from Sindoh (Seoul, South
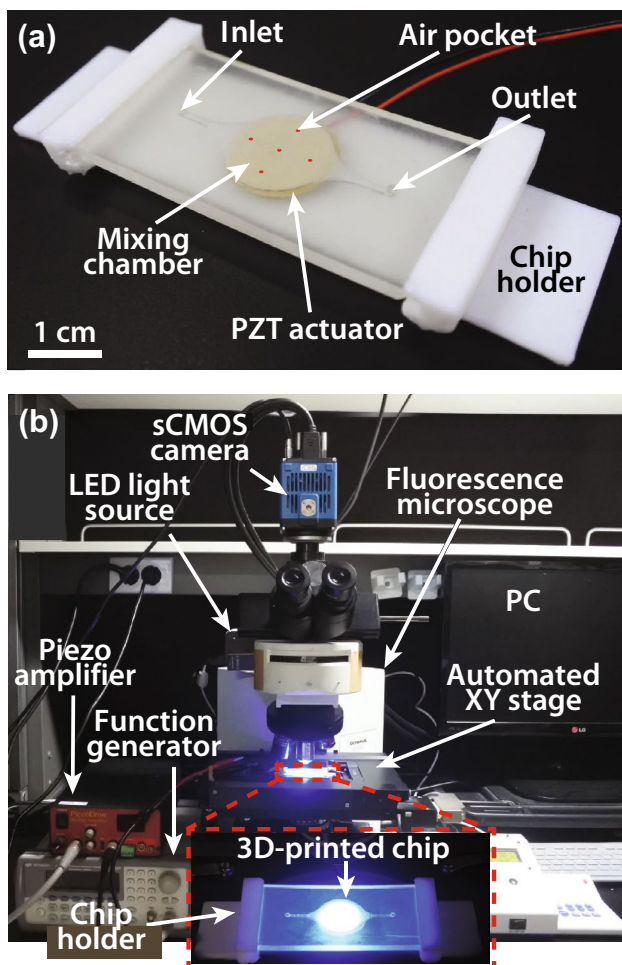
**Fig. 5** Experimental setup. **a** A 3D-printed custom jig is used to clamp a micromixer chip. The vertically arranged air pockets are colored in red for visualization. **b** The chip was placed on a motorized stage of an upright epifluorescence microscope, equipped with an sCMOS camera and an LED light source. The PZT actuator bonded to the chip is connected to a piezo amplifier and function generator for bubble excitation and cavitation microstreaming

Korea). The shorter edges of the chip were clamped for the maximum vibration. The bonded PZT actuator was connected to an impedance analyzer MFIA (Zurich Instruments, Zurich, Switzerland). Impedance plots obtained in the frequency range of 1–10 kHz enabled us to locate the resonance frequency (i.e., the frequency exhibiting the maximum magnitude difference between the resonance and anti-resonance $\Delta|Z|$, and the highest phase peak $\Delta\theta$). For more details on the EMIS-based determination of resonance frequency, see Ref. [74].

For streamline imaging, the chip was mounted on a motorized stage (PZ-2000FT, Applied Scientific Instrumentation, Eugene, OR, USA) in an upright fluorescence microscope BX50 (Olympus) equipped with an sCMOS camera PCO.EDGE 5.5 (PCO, Kelheim, Germany) and

Metamorph software (Molecular Devices, San Jose, California, United States), as shown in Fig. 5b. The micromixer chip was filled with 25% (v/v) diluted solution of 10-µm fluorescence microbeads (Spherotech), and the inlet/outlet ports were sealed using Teflon tape. The PZT actuator was excited at a measured resonance frequency with a 60 $V_{pp}$ sinusoidal signal, which is generated by a function generator (33210A, Keysight, Santa Rosa, California, United States) and a piezo amplifier (PD200, PiezoDrive, Newcastle, Australia). Motion images were captured using a $2\times$ objective lens (Plan, Olympus) through the top plate (i.e., treated surface) at 100 frames per second. Among the recorded images, ten frames were selected after cavitation microstreaming had reached a steady state. The streamlines were synthesized from the selected images using ImageJ and FlowTrace plug-in. For validation of our 3D-printing and surface-treatment method, two types of micromixer chips were tested: a control chip, 3D-printed under an unoptimized condition (i.e., condition from Step 2, Sect. 2.3) and a chip 3D-printed and treated under an optimized condition (i.e., condition from Step 7, Sect. 2.4). The streamline patterns acquired for both chips were compared for the viability of imaging-based microfluidic applications.

## 3 Results and Discussion

### 3.1 Determination of 3D-Printing Conditions

For the experiment in Step 1, three slide-cover chips were printed using three different resins: PlasCLEAR, GR-10, and PR48 (Fig. 6, upper panel). Resolutions determined by the low-resolution USAF 1951 test target through the slide-cover chips were 143.7 lp/mm (group 7—element 2, red box) for PR48, whereas the resolutions for both PlasCLEAR and GR-10 were 80.6 lp/mm (group 6—element 3, red box).

Each resin has a different formulation of the monomer/oligomer, photoinitiator, photoabsorber, and reactive diluent [35, 82–84]. For example, PlasCLEAR contains *7,7,9 (or 7,9,9)-trimethyl-4,13-dioxo3,14-dioxa-5,12-diazahexadecane-1,16-diyl bismethacrylate* and *tetrahydrofurfuryl methacrylate* [85], whereas PR48 has Sartomer SR 494 and Allnex Ebecryl 8210 [35]. Although it is unclear, we speculate that different compositions may result in dissimilar optical properties of the photopolymerized resin in terms of light transmission or scattering [57]. Fluorescence images (lower panel) confirmed the superior resolution of PR48, a mediocre resolution of PlasCLEAR, and an unacceptable resolution of GR-10. Higher background fluorescence of the PR48 than that of PlasCLEAR was observed, possibly due to stronger autofluorescence of the resin [7, 86, 87]. Consequently, the best resolving resin was PR48, and we chose this resin for subsequent determination steps.
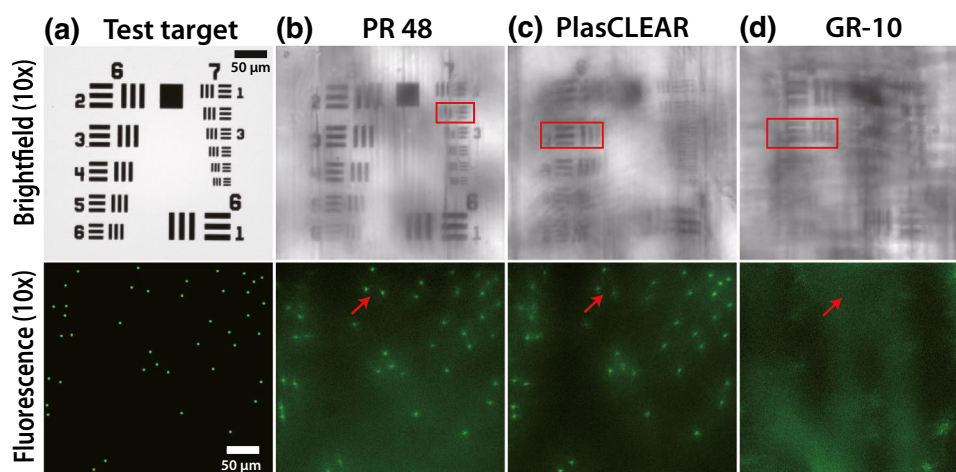
**Fig. 6** Comparison of brightfield (upper panels) and fluorescence images (lower panels) against images of **a** a USAF 1951 target and fluorescence beads, captured through cover-slide chips printed using three different resins **b** PR48, **c** PlasCLEAR, and **d** GR-10. Red boxes represent the resolutions determined through image analysis. Red arrows indicate fluorescence beads which are used to distinguish the image quality over the other resins. PR48 shows the best resolution compared to those of PlasCLEAR and GR-10

For the result of Step 2 (Fig. 7), two chips were printed in two different build orientations (i.e., top-up and top-down, see Fig. 3) with the printing conditions determined from Step 1. For the top-down orientation, an additional 4× brightfield image (groups 4–5) was captured because resolution could not be measured with 10× images (groups 6–7). The resolutions of 143.7 lp/mm (groups 7—element 2) and 17.96 (group 4—element 2) were measured for the top-up and top-down orientations, respectively (upper panel).

Significant overcuring (i.e., 80-µm offset for 25-µm layer thickness) may have created roughened polymerized resins overhung to the ceiling, which reduced light transmission and increased scattering (Fig. 7c). Random microscale surface features rendered the investigation of standard patterns challenging, as can be seen in both 10× and 4× images. Additionally, the significant scratches and blemishes replicated from the vat window adversely affected the captured images. Furthermore, it was impossible to observe fluorescent beads through the top-down-orientation chip (lower panel). Taken together, the resolution for the top-up orientation was significantly better than that
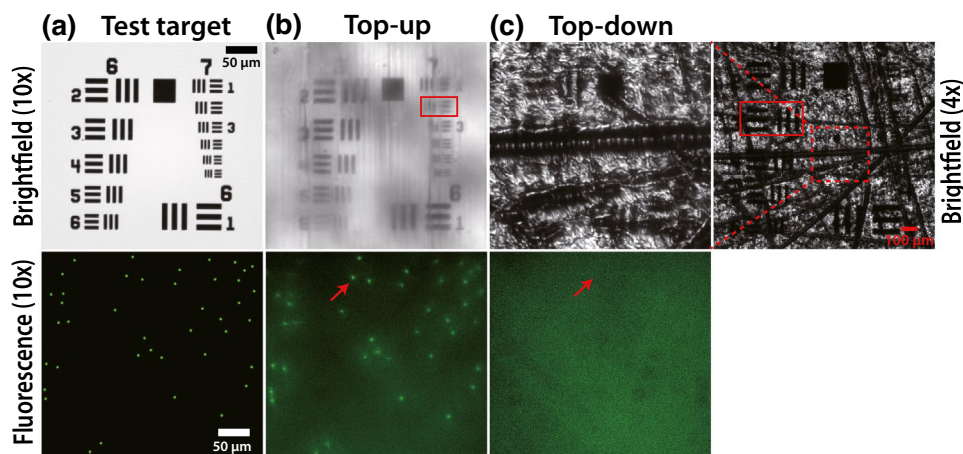


**Fig. 7** Comparison of brightfield (upper panels) and fluorescence images (lower panels) against images of **a** a USAF 1951 target and fluorescence beads, captured through cover-slide chips printed using two different build orientations: **b** top-up and **c** top-down (an additional 4× image was included because the resolution could not be measured with the 10× image). Red boxes represent the resolutions determined through image analysis. Red arrows indicate fluorescence beads which are used to distinguish the image quality over the other build orientation. The top-up orientation exhibits a superior resolution compared to that of the top-down orientation. None of the fluorescent beads were recognizable for the top-down orientation

of the top-down orientation. Therefore, this orientation was selected for subsequent steps.

In the experiment for Step 3, four chips with layer thicknesses of 10, 25, 50, and 100 μm were printed using the build condition transferred from Step 2. The resolutions were 90.5 (group 6—element 4), 143.7 (group 7—element 2), 181.0 (group 7—element 4), and 114.0 lp/mm (group 6—element 6), respectively (Fig. S2 in SI, upper panel). A layer thickness of 50 μm yielded the best resolution, followed by 25 μm.

The layer-thickness and layer-offset parameters chiefly affect the thicknesses of a sliced layer and the interface between sliced layers, as well as the distribution of cross-linking density in layer bodies and interfaces [58]. These variations in the thickness and cross-linking density could cause different light transmissions. Heterogeneous refractive index (RI) [7] and varying transparency across a layer body and interfaces were observed in SLA-printed samples [32, 57, 88]. Such variations in optical properties across the Z direction of the top plate may have contributed to the difference in the optical resolutions of the cover chips printed with varying layer thicknesses. The image of fluorescence beads for the 50 μm case was also the sharpest (lower panel). Therefore, a layer thickness was set to 50 μm for subsequent steps.

For the experiment in Step 4, four chips were prepared with layer offsets of 2.5, 7.5, 12.5, and 25 μm (5%, 15%, 25%, and 50% of the layer thickness of 50 μm determined from Step 3) while other printing parameters were transferred from Step 3. The measured resolutions were 181.0 (group 7—element 4), 114.0 (group 6—element 6), 203.2 (group 7—element 5), and 128.0 lp/mm (group 7—element 1), respectively (Fig. S3 in SI, upper panel). The offset of 12.5 μm yielded the best resolution, followed by 2.5 μm.

The offset is the additional light energy illuminated during the photopolymerization of a layer to enhance adhesion to the preceding layer. The increasing light energy $I_o$ increases the penetration depth $C_d$ [31, 34, 57, 58, 89] and the overall distribution of cumulative light dosage across the layer bodies and interfaces [34, 57] because of sequential exposure to UV light for polymerization of the succeeding layers. Therefore, the cross-linking density across the printed layers and interfaces and the relevant optical properties can vary in the Z direction. Such variations in the optical properties of the top plate may have contributed to a difference in the resolution of the cover chips printed with different offset values. Together with the layer thickness, the offset is a critical parameter that should be optimized, especially when printing overhanging structures such as the ceilings and covers of microfluidic channels and cavities [12, 26, 57, 70]. The image of fluorescence beads for the 12.5 μm case was also the sharpest (Fig. S3 in SI, lower

panel). Consequently, a layer offset of 12.5 μm was selected for the subsequent steps.

The top plate of the slide-cover chip printed using the conditions determined in Step 4 was thicker than the original design (614 μm vs. 450 μm) because the build-plate thickness was larger (170 μm vs. 50 μm), possibly due to the long burn-in exposure time (16 s, Sect. 2.3). This means that the actual top-plate thickness was 444 μm, which is an 11% increase from the design. Dimensional changes of DLP-SLA printing depending on printing parameters have been well documented [26]. The thickness was measured using a vernier caliper (CD-P20M, Mitutoyo, Kawasaki, Japan).

## 3.2 Optimization of Surface-Treatment Condition

For Step 5 (Fig. 8), we printed four cover chips using the predetermined conditions in Step 4 (Sect. 3.1). We initially employed a 10× objective lens (UPlanFL, Olympus) and the low-resolution USAF 1951 target (Thorlabs, groups 2–7). However, the resolution was virtually indistinguishable after grinding with a 1000 grit sandpaper. The identical resolution of 181.0 lp/mm was obtained for 2000–5000 grit cases. Thus, we switched to the high-resolution target (Graticules Optics, groups 2–9) and a 40× objective lens (UPLanFL) to discern resolution-pattern images generated with different sanding conditions and subsequent surface-treatment steps (i.e., polishing and RI-matching coatings).

With the new target and lens, an improvement in the resolution (upper panel) was observed because of the cumulative effect of sanding the top surface (initially marred by the anodized surface of the build platform [7, 26, 35]) with progressively finer sandpapers from 1000 to 5000 grits. As the grit number increased, the resolution pattern images turned crisp. The resolution through the slide-cover chip that was cumulatively polished using sandpapers of grits 1000, 200, 3000, and 5000 for 5 min each was 181.0 lp/mm (group 7—element 4), 512.0 lp/mm (group 9—element 1), 645.1 lp/mm (group 9—element 3), and the equal 645.1 lp/mm, respectively. The resolution for the 1000-grit sandpaper case deteriorated from that of the case for non-treated case (the best case of Step 4, 203.2 lp/mm), possibly due to scratches resulting from 1000-grit sanding. It was difficult to distinguish the results from both 3000- and 5000-grit cases even with the high-resolution USAF target (upper panel). The fluorescence images of the microbeads were also indistinguishable for both cases (lower panel). Therefore, we resorted to the contrast value (middle panel) obtained from intensity plots of the highest resolution pattern (group 9—element 3). The average contrast values, calculated using Eq. (1) for the horizontal and vertical patterns, increased from 6.43 to 7.31% as the grit number increased, indicating the 5000-grit case had the best optical quality. Therefore, the best sanding condition was 5 min of consecutive polishings with all four
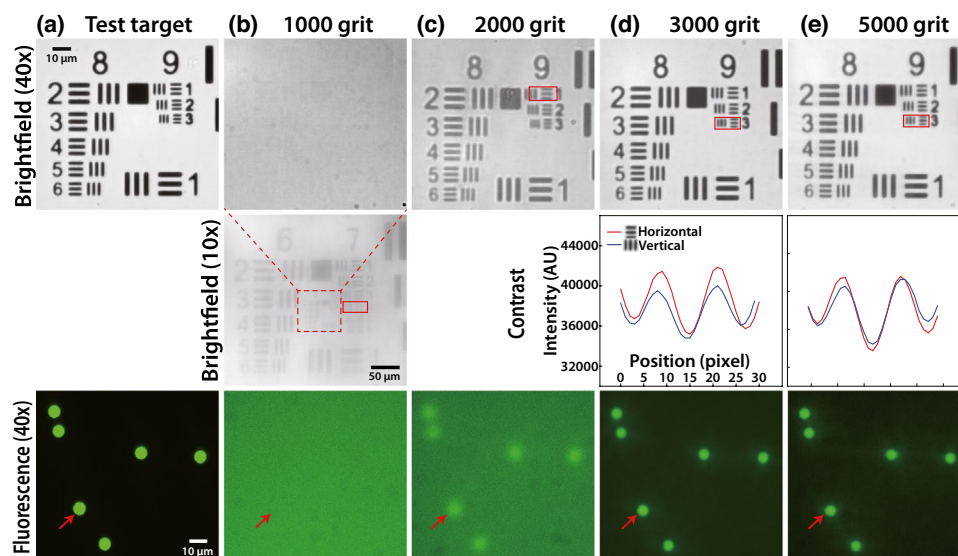
**Fig. 8** Comparison of brightfield (upper panels) and fluorescence images (lower panels) against images of **a** a USAF 1951 target and fluorescence beads, captured through slide-cover chips treated with consecutive wet sanding using **b** 1000, **c** 2000, **d** 3000, and **e** 5000 grit sandpapers for 5 min each. The images were captured using a 40× objective lens (UPlanFL, Olympus). An additional brightfield image for the 1000 grit case was taken using the 10× objective lens because resolution could not be measured using the 40× image. Red boxes represent the resolutions determined through the image analysis. Red arrows indicate fluorescence beads which are used to distinguish the image quality over the other sanding conditions. Due to indistinguishable resolution, the intensity of horizontal (red) and vertical (blue) resolution patterns for the 3000- and 5000-grit cases was plotted, and their contrast values were measured (middle panels). Four consecutive sanding with increasingly higher grit sandpapers shows the best optical quality

sandpapers, and this condition was employed in the subsequent surface-treatment steps.

The thickness of the top plate was progressively reduced from 614 μm (from Step 4) because of material removal during sanding: 576, 544, 494, and 488 μm for 1000, 2000, 3000, and 5000 grit sandpapers, respectively. Such thickness variation of a cover chip may affect optical resolution and contrast to some degree [90], although surface roughness mainly influences optical quality due to light diffraction and scattering [8, 28, 29]. It is challenging to decouple this thickness impact on the overall optical-quality enhancement from the effects of the surface-finish improvement; the resolution worsened when the thickness reduction was largest (after sanding with a 1000 grit sandpaper), although the contrast and resolution generally improved as the thickness decreased. Further study in the future may be required to decouple the impacts of thickness and surface finish on the overall optical quality.

For the Step 6 experiment (Fig. S4 in SI), four cover chips were printed using the conditions determined from Step 4. Then the top surfaces were sanded using the condition determined from Step 5. Then, the top surfaces were polished using a 50-nm alumina slurry for progressively longer durations of 5, 10, 15, and 20 min. As in a previous report where the diamond paste was used [34, 86], a mild optical-quality improvement was observed due to the cumulative effect of alumina polishing on the top surface. As the polishing time increased, the resolution patterns appeared marginally sharper, but it was difficult to clearly distinguish them. The images of the upper panel indicate that the resolution through the cover chips polished for 5, 10, 15, and 20 min was identical: 645.1 lp/mm. The sharpness of fluorescence microbead images was also indistinguishable even with increasing polishing times (lower panel). Therefore, we plotted intensity and characterized contrast for each polishing case (middle panel). The average contrast values for the horizontal and vertical patterns were 3.30, 7.69, 8.34, and 9.60% for the polishing time of 5, 10, 15, and 20 min, respectively. The best condition for the highest contrast value was 20-min polishing, and this condition was employed in the remaining surface-treatment step.

The thickness of the top plate was slightly reduced from 488 to 458 μm throughout the cumulative polishing step. The thickness reduction was 6.1%, while the contrast was increased 31.3% (from 7.31 to 9.6%). Therefore, the impact of thickness reduction on contrast improvement seemed marginal, but further study may be required to decouple this impact on the overall optical-quality enhancement from the effects of surface roughness. However, the dimensional changes after printing [26] and thickness reduction observed throughout Steps 5 and 6 should be considered when designing a microfluidic device (e.g., overdesign). For example, an extra thickness of 164 μm (i.e., the difference between the designed thickness and measured thickness) observed here

can be used as a buffer for the thickness reduction resulting from the surface treatment.

In the last step (Step 7), we attempted to further smooth the top surface by coating with a RI-matching film: silicone oil ($n = 1.51$), sandalwood oil ($n = 1.51$–$1.52$), and PR48 resin ($n = 1.5$–$1.52$, after polymerization). Four cover chips were printed with the conditions determined from Step 4, and then sanded and polished using the conditions obtained from Steps 5 and 6, respectively. Thin oil layers (silicone and sandalwood oils) were applied to the polished surface as a "liquid" film, whereas the coated PR48 resin was photopolymerized to form a solid film to match the RI more accurately. A chip was left untreated as a negative control.

The upper panel images of Fig. 9 shows randomly distributed darker spots (e.g., on the horizontal pattern of group 8—element 1 for the resin-coating case), which may be stemmed from uneven distribution of coatings (i.e., thicker regions absorb more light). The test target images display no noticeable improvement in resolution compared to that of the control. Therefore, the intensity plots for all four cases were generated and analyzed. We observed a decrease in the average contrast values for all three treated cases, in the following order: silicone oil (27.63%), sandalwood oil (19.91%), PR48 resin (15.89%), and the untreated control case (9.60%). The reason for this decrease remains unclear at the moment, but the silicone oil ($n = 1.51$) could match RI better than the other coatings. The fluorescence images of the microbeads were indistinguishable in terms of sharpness (lower

panel). However, we noted that background fluorescence varied over different coatings. Sandalwood oil, extracted from natural sandalwood, may have more impurities that can yield stronger autofluorescence than the synthetic silicone oil. For the PR48 resin case, an increase in the overall top-plate thickness (458 vs. 512 μm) after polymerization can absorb more light and generate more autofluorescence. Coating with silicone oil may help to improve the quality of fluorescence imaging because background fluorescence is the smallest compared to the other cases. Considering the highest contrast, the best coating material was silicone oil. We selected this final condition for the post-printing treatment of a proof-of-concept micromixer chip.

## 3.3 Summary of Step-Wise Determination of 3D-Printing and Surface-Treatment Conditions

The step-wise determination of the build (Sect. 3.1) and surface-treatment conditions (Sect. 3.2) is summarized in Table 1. The boldfaced items indicate the established parameter value and the corresponding resolution for each step. As described in Experimental Section, the initial build parameters for Step 1 were a light intensity of 30 mW/cm$^2$, a layer thickness of 25 μm, and a layer offset of 80 μm for all resins. The exposure times were 6.3 s for PlasCLEAR, 0.305 s for GR-10, and 2.0 s for PR48. The number of burn-in layers (build plates) was one, and the
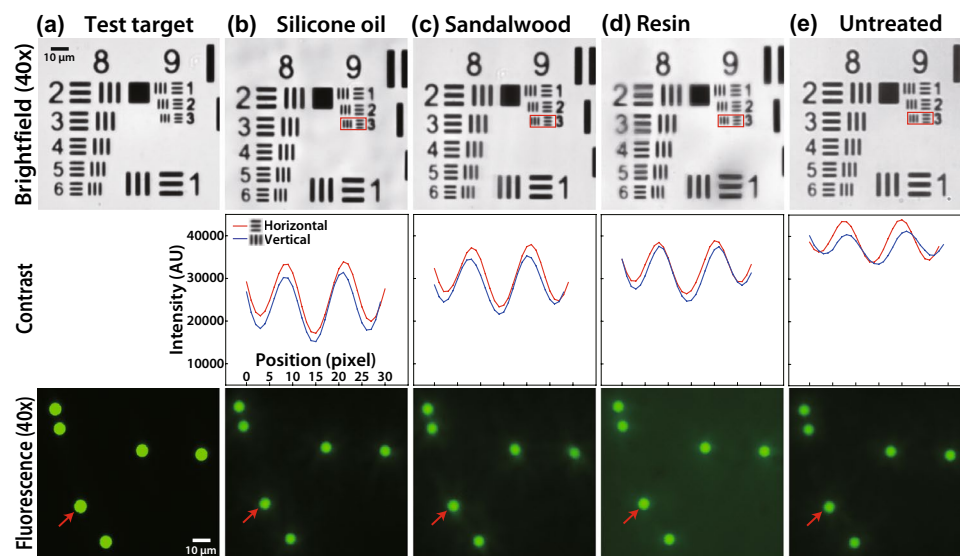


**Fig. 9** Comparison of brightfield (upper panels) and fluorescence images (lower panels) against images of **a** a USAF 1951 target and fluorescence beads, captured through slide-cover chips using different coatings of **b** silicone oil, **c** sandalwood oil, **d** PR48 resin, and **e** untreated (control). Red boxes represent the resolutions determined through the image analysis. Red arrows indicate fluorescence beads which are used to distinguish the image quality over the other coating conditions. Resolution cannot be distinguished from the brightfield images. For contrast comparison, intensity values for horizontal (red) and vertical (blue) resolution patterns are plotted for each coating case (middle panels). The silicone oil case (control) yields the best optical quality based on the average contrast value for the horizontal and vertical patterns

**Table 1** Summary of step-wise determination of 3D-printing and surface-treatment conditions

|  |  | Sample #1 | Sample #2 | Sample #3 | Sample #4 |
|---|---|---|---|---|---|
| 1. Resin type (Fig. 6) | Parameter | GR-10 (Pro3dure) | PlasCLEAR (Asiga) | PR48 (Autodesk) |  |
|  | Resolution (lp/mm) | 80.6 | 80.6 | **143.7** |  |
| 2. Build orientation (Fig. 7) | Parameter | **Top-up** | Top-down |  |  |
|  | Resolution (lp/mm) | **143.7** | 90.5 |  |  |
| 3. Layer thickness (Fig. S2 in SI) | Parameter | 10μm | 25μm | **50μm** | 100μm |
|  | Resolution (lp/mm) | 90.5 | 143.7 | **1813** | 114.0 |
| 4. Layer offset (Fig. S3 in SI) | Parameter | 2.5μm | 7.5μm | **12.5μm** | 25μm |
|  | Resolution (lp/mm) | 181.0 | 114.0 | **203.2** | 128.0 |
| 5. Sanding (Fig. 8) | Parameter | 1000 grit | 2000 grit | 3000 grit | **5000 grit** |
|  | Resolution (lp/mm) | 181.0 | 228.1 | 228.1 | **228.1** |
|  | Contrast (%) |  |  | 6.43 | **7.31** |
| 6. Alumina polishing (Fig. S4 in SI) | Parameter | 5 min | 10 min | 15 min | **20 min** |
|  | Resolution (lp/mm) | 228.1 | 228.1 | 228.1 | **228.1** |
|  | Contrast (%) | 3.30 | 7.69 | 8.34 | **9.60** |
| 7. Refractive-index (RI) matching (Fig. 9) | Parameter | **Silicone oil** | Sandalwood oil | Resin coating | No treatment |
|  | Resolution (lp/mm) | **228.1** | 228.1 | 228.1 | 228.1 |
|  | Contrast (%) | **27.63** | 19.91 | 15.89 | 9.60 |

Boldfaced items indicate the determined parameter value and the corresponding resolution for each determination step

thickness was 50 μm for all resins. The burn-in exposure time was 17.3 s for PlasCLEAR, 0.8 s for GR-10, and 16 s for PR48. The heater temperature was set to 25 °C, and the build orientation was top-up. The printing parameters determined from Step 1 were transferred to Step 2 including the selected resin type (i.e., PR48). The printing parameters for Step 2 were carried over to Step 3 including build orientation (top-up). The updated build parameters, including a layer thickness of 50 μm were passed on to Step 4. This type of parameter carryover was repeated until the last step (Step 7).

Our parameter-determination process may not be globally optimal. However, a global search would be significantly time-consuming in seven-dimensional parameter space. In this communication, we successfully pioneered an experimental, systematic, and quantitative approach to determine the 3D-printing and surface-treatment conditions using USAF 1951 resolution test targets, adapted from optics and optical engineering [46–49]. We achieved a drastic increase in the resolution from 80.6 to 645.1 lp/mm (i.e., the line width of the standard pattern from 6.2 to 0.78 μm) through the proposed determination process. The final 3D-printing and surface-treatment conditions were as follows: (1) PR48 resin, (2) top-up build orientation, (3) layer thickness of 50 μm, (4) layer offset of 12.5 μm, (5) four consecutive sandings using 1000, 2000, 3000, and 5000 grit sandpapers for 5 min each, (6) 20 min polishing with alumina slurry, and (7) silicone-oil coating. This fabrication and post-printing treatment were successfully employed to prepare our micromixer chip.

## 3.4 Cavitation Microstreaming and Streamline Visualization for Micromixing Applications

We manufactured two micromixer chips to validate our approach: one printed with an under-optimized condition (i.e., condition from Step 2) and the other with semi-optimized condition (i.e., condition from Step 7). It is critical to 3D-print mixer chips in the top-up orientation because overcured surfaces under the ceiling significantly interfere with optical imaging through the top plate using an upright microscope. The build orientation should be reversed, and the bottom surface should be treated when imaging through the bottom plate using an inverted microscope. The overall chip microfabrication time was 45 min for the under-optimized case (no surface treatment) and 121 min for the semi-optimized case (including times for sandpapering, alumina polishing, cleaning of sanding and polishing residues, and coating of silicone oil). The durations for both cases include 3D printing, removing from the vat, clearing the mixing chamber and microchannels using isopropanol inside an ultrasonic bath, and UV curing.

The resonance frequencies of these chips, measured individually using our EMIS method, were 5.0 and 5.3 kHz, respectively [74, 77]. After injecting diluted fluorescent-bead solutions, two chips were excited at these predetermined frequencies. We observed a strong bending mode vibration in each agitated chip, which is essentially a mechanical structure similar to a thin edge-supported beam [74, 77].

As shown in Fig. 10a, it was extremely difficult to visualize cavitation microstreaming from the oscillating bubble trapped in the central air pocket of the under-optimized chip because the streamlines were obscured by random fluorescence patterns (possibly stemming from the rough top surface). A hint of bead movement was observed in the video clip synthesized using acquired image frames (see Supplementary Materials, Video Clip #1). For the semi-optimized chip (Fig. 10b), we clearly observed streamlines that emanated from the vibrating bubble as circulatory flow fields (see Supplementary Materials, Video Clip #2). The flow visualization of the cavitation microstreaming phenomena is critical for determining operating conditions of micromixers that rely on oscillating bubbles because longer and broader streamlines yield better mixing [74, 77].

This result confirms a significant improvement in the optical quality of the microfluidic device prepared using our proposed approach. Many previous micromixers based on cavitation microstreaming were fabricated using
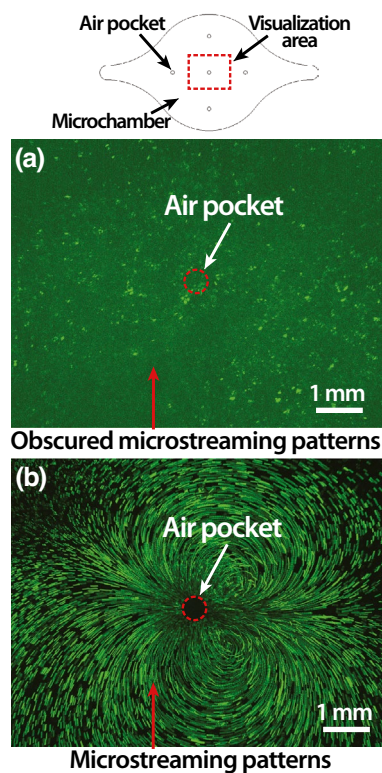


**Fig. 10** Streamlines generated from high-speed motion images of an oscillating bubble captured inside a central air pocket of the micromixer chip (visualization area). **a** The under-optimized chip was prepared using the 3D-printing condition determined from Step 2. Microstreaming patterns were obscured by the top plate of unacceptable optical quality (see Supplementary Materials, Video Clip #1). **b** The semi-optimized chip was prepared using the 3D-printing and surface-treatment conditions determined from Step 7. Microstreaming patterns were clearly observed through the micromixer chip (see Supplementary Materials, Video Clip #2)

time-consuming multilayer PDMS bonding, which requires cleanroom or foundry service for master-mold fabrication (takes up to a few days, including master-mold manufacturing and chip fabrication) [78, 81, 91, 92]. Some cleanroom-free techniques such as $CO_2$-laser cutting [74, 77] or machining (e.g., micro milling) of PMMA or polycarbonate [79, 93], followed by multilayer bonding, could require a shorter time compared to our approach. This is because surface treatment is not required (clean top or bottom surfaces), and the chip can be directly fabricated from a CAD design similarly with 3D printing. However, the feature resolution is considerably worse for laser cutting (~ 200 μm vs. ~ 27 μm) [74, 77], and the initial tooling/setting-up time and cost are high for machining [8, 94]. The manual bonding of multiple layers can also lower the fabrication yield (i.e., the rate of successful fabrications without leakage) and can cause significant manufacturing variability [6, 8, 12, 26]. In contrast, our 3D-printing process transforms a CAD design into a complete, operational chip in 121 min at an adequate fabrication accuracy (nominal *XY* resolution of ~ 27 μm and *Z* resolution of ~ 1 μm) after minor surface treatments. Although not demonstrated in this work, interfacing with a 3D-printed microfluidic chip is more standardized, straightforward, and secure than those of laser cut or machined microfluidic chips [3, 6, 8, 11–13]. Taken together, our approach of reliable and rapid 3D printing and surface treatment presented in this communication can accelerate the research, development, and production of microfluidic chips with optical imaging or detection applications for academia or start-ups.

## 4 Conclusion

The DLP-SLA 3D printing has been recently under the spotlight in the microfluidics community because of (1) direct manufacturing of a microfluidic chip from a digital CAD design, (2) rapid iteration of chip design and fabrication, (3) relatively high printing resolution, (4) cleanroom-free fabrication, (5) affordable instrument/manufacturing costs, and (6) polymer materials similar to those used in mass production (e.g., injection molding). However, there is still room for improvement in DLP-SLA printing, including biocompatibility, multi-material-printing capability, and manufacturability of a long, narrow, complicated microfluidic network. More importantly, optical quality is one of the critical limitations that must be addressed for DLP-SLA printing to be used routinely because optical detection and/or observation are common for microfluidic devices.

We opted for relatively straightforward sanding, alumina polishing, and RI matching to improve optical quality, instead of relying on time-consuming, empirical, and often unsafe approaches including solvent-fume polishing, various coatings (PDMS, PS, epoxy, acrylic spray, and lacquer), and printing

on a glass/plastic slide. A key contribution of our work is the methodological and quantitative determination of 3D-printing and surface-treatment conditions performed using a resolution measurement technique based on the USAF 1951 resolution target, which is a well-proven tool in optics and optical engineering fields. By step-wise determination of printing and surface-treatment conditions (i.e., resin type, build orientation, layer thickness, layer offset, sandpaper grit number, alumina polishing duration, and RI-matching coating types), we were able to significantly improve the resolution of the slide-cover chip from 80.6 to 645.1 lp/mm (i.e., the line width of the standard pattern from 6.2 to 0.78 μm), and the contrast from 3.30 to 27.63% for 645.1 lp/mm resolution.

Our fabrication approach was successfully validated using a working microfluidic device, which is a micromixer based on cavitation microstreaming. In the control experiment, cavitation microstreaming could not be observed because of the unacceptable optical quality of the top plate, indicating an obvious limitation of unoptimized 3D printing. However, streamlines emanating from an oscillating bubble were clearly observed through the microfluidic chip prepared using semi-optimized printing and surface-treatment conditions. The visualization of streaming patterns is essential for designing air pockets and determining the operating conditions of the cavitation-microstreaming mixer. The overall fabrication time from a CAD design to a complete chip was only 2 h, including all post-printing processes.

Our results indicate that a relatively rapid design iteration of microfluidic devices is possible using a systematically, optically, quantitatively optimized DLP-SLA 3D-printing and surface-treatment method. We are currently improving our approach using higher magnification optics and design-of-experiment (DOE) in the direction of reducing fabrication time while improving optical quality. The fabrication of a 3D-printed DNA-extraction and detection device, a continuation of our previous work [77], is also underway.

## Declarations

**Conflict of interest** The authors declare no competing financial interests.

## References

1. Gross, B.C., Erkal, J.L., Lockwood, S.Y., Chen, C., Spence, D.M.: Evaluation of 3D printing and its potential impact on biotechnology and the chemical sciences. Anal. Chem. **86**, 3240–3253 (2014)
2. Waheed, S., Cabot, J.M., Macdonald, N.P., Lewis, T., Guijt, R.M., Paull, B., Breadmore, M.C.: 3D printed microfluidic devices: enablers and barriers. Lab Chip **16**, 1993–2013 (2016)
3. Au, A.K., Huynh, W., Horowitz, L.F., Folch, A.: 3D-printed microfluidics. Angew. Chem. Int. Ed. **55**, 3862–3881 (2016)
4. Dixit, C., Kadimisetty, K., Rusling, J.: 3D-printed miniaturized fluidic tools in chemistry and biology. Trends Anal. Chem. **106**, 37–52 (2018)
5. Amin, R., Knowlton, S., Hart, A., Yenilmez, B., Ghaderinezhad, F., Katebifar, S., Messina, M., Khademhosseini, A., Tasoglu, S.: 3D-printed microfluidic devices. Biofabrication **8**, 022001 (2016)
6. Naderi, A., Bhattacharjee, N., Folch, A.: Digital manufacturing for microfluidics. Annu. Rev. Biomed. Eng. **21**, 325–364 (2019)
7. Rank, M., Sigel, A., Bauckhage, Y., Suresh-Nair, S., Dohmen, M., Eder, C., Berge, C., Heinrich, A.: 3D printing of optics based on conventional printing technologies. In: 3D Printing of Optical Components, pp. 45–167. Springer, Berlin (2021)
8. Bhattacharjee, N., Urrios, A., Kang, S., Folch, A.: The upcoming 3D-printing revolution in microfluidics. Lab Chip **16**, 1720–1742 (2016)
9. Wang, L., Pumera, M.: Recent advances of 3D printing in analytical chemistry: focus on microfluidic, separation, and extraction devices. Trends Anal. Chem. **135**, 116151 (2021)
10. Mehta, V., Rath, S.N.: 3D printed microfluidic devices: a review focused on four fundamental manufacturing approaches and implications on the field of healthcare. Bio-Des. Manuf. **4**, 1–33 (2021)
11. Yazdi, A.A., Popma, A., Wong, W., Nguyen, T., Pan, Y., Xu, J.: 3D printing: an emerging tool for novel microfluidics and lab-on-a-chip applications. Microfluid. Nanofluid. **20**, 50 (2016)
12. Chan, H.N., Tan, M.J.A., Wu, H.: Point-of-care testing: applications of 3D printing. Lab Chip **17**, 2713–2739 (2017)
13. Capel, A.J., Rimington, R.P., Lewis, M.P., Christie, S.D.: 3D printing for chemical, pharmaceutical and biological applications. Nat. Rev. Chem. **2**, 422–436 (2018)
14. Macdonald, N.P., Cabot, J.M., Smejkal, P., Guijt, R.M., Paull, B., Breadmore, M.C.: Comparing microfluidic performance of three-dimensional (3D) printing platforms. Anal. Chem. **89**, 3858–3866 (2017)
15. Nielsen, A.V., Beauchamp, M.J., Nordin, G.P., Woolley, A.T.: 3D printed microfluidics. Annu. Rev. Anal. Chem. **13**, 45–65 (2020)
16. Beauchamp, M.J., Nordin, G.P., Woolley, A.T.: Moving from millifluidic to truly microfluidic sub-100-μm cross-section 3D printed devices. Anal. Bioanal. Chem. **409**, 4311–4319 (2017)
17. Au, A.K., Bhattacharjee, N., Horowitz, L.F., Chang, T.C., Folch, A.: 3D-printed microfluidic automation. Lab Chip **15**, 1934–1941 (2015)
18. Lim, J.W., Kim, T.-Y., Lim, M.-C., Choi, S.-W., Woo, M.-A.: Portable pumpless 3D-printed chip for on-site colorimetric screening of Hg 2+ in lake water. Biochip J. **14**, 169–178 (2020)
19. Aladese, A.D., Jeong, H.-H.: Recent developments in 3D printing of droplet-based microfluidics. Biochip J. **15**, 1–21 (2021)
20. Ho, C.M.B., Ng, S.H., Li, K.H.H., Yoon, Y.-J.: 3D printed microfluidics for biological applications. Lab Chip **15**, 3627–3637 (2015)
21. He, Y., Wu, Y., Fu, J.Z., Gao, Q., Qiu, J.J.: Developments of 3D printing microfluidics and applications in chemistry and biology: a review. Electroanalysis **28**, 1658–1678 (2016)
22. Xiao, R., Li, X., Jia, H., Surjadi, J.U., Li, J., Lin, W., Gao, L., Chirarattananon, P., Lu, Y.: 3D printing of dual phase-strengthened microlattices for lightweight micro aerial vehicles. Mater. Des. **206**, 109767 (2021)
23. Kara, A., Vassiliadou, A., Ongoren, B., Keeble, W., Hing, R., Lalatsa, A., Serrano, D.R.: Engineering 3D printed microfluidic

chips for the fabrication of nanomedicines. Pharmaceutics **13**, 2134 (2021)

24. Tzivelekis, C., Selby, M.P., Batet, A., Madadi, H., Dalgarno, K.: Microfluidic chip fabrication and performance analysis of 3D printed material for use in microfluidic nucleic acid amplification applications. J. Micromech. Microeng. **31**, 035005 (2021)

25. Au, A.K., Lee, W., Folch, A.: Mail-order microfluidics: evaluation of stereolithography for the production of microfluidic devices. Lab Chip **14**, 1294–1301 (2014)

26. Beckwith, A.L., Borenstein, J.T., Velásquez-García, L.F.: Monolithic, 3D-printed microfluidic platform for recapitulation of dynamic tumor microenvironments. J. Microelectromech. Syst. **27**, 1009–1022 (2018)

27. Chen, C., Mehl, B.T., Munshi, A.S., Townsend, A.D., Spence, D.M., Martin, R.S.: 3D-printed microfluidic devices: fabrication, advantages and limitations—a mini review. Anal. Methods **8**, 6005–6012 (2016)

28. Urrios, A., Parra-Cabrera, C., Bhattacharjee, N., Gonzalez-Suarez, A.M., Rigat-Brugarolas, L.G., Nallapatti, U., Samitier, J., DeForest, C.A., Posas, F., Garcia-Cordero, J.L.: 3D-printing of transparent bio-microfluidic devices in PEG-DA. Lab Chip **16**, 2287–2294 (2016)

29. Bhattacharjee, N., Parra-Cabrera, C., Kim, Y.T., Kuo, A.P., Folch, A.: Desktop-stereolithography 3D-printing of a poly (dimethylsiloxane)-based material with sylgard-184 properties. Adv. Mater. **30**, 1800001 (2018)

30. Monzón, M., Ortega, Z., Hernández, A., Paz, R., Ortega, F.: Anisotropy of photopolymer parts made by digital light processing. Materials **10**, 64 (2017)

31. Kowsari, K., Zhang, B., Panjwani, S., Chen, Z., Hingorani, H., Akbari, S., Fang, N.X., Ge, Q.: Photopolymer formulation to minimize feature size, surface roughness, and stair-stepping in digital light processing-based three-dimensional printing. Addit. Manuf. **24**, 627–638 (2018)

32. Mostafa, K.G., Nobes, D.S., Qureshi, A.J.: Investigation of light-induced surface roughness in projection micro-stereolithography additive manufacturing (PμSLA). Procedia CIRP **92**, 187–193 (2020)

33. Sun, C., Fang, N., Wu, D., Zhang, X.: Projection micro-stereolithography using digital micro-mirror dynamic mask. Sens. Actuators A Phys. **121**, 113–120 (2005)

34. van der Linden, P.J.E.M., Popov, A.M., Pontoni, D.: Accurate and rapid 3D printing of microfluidic devices using wavelength selection on a DLP printer. Lab Chip **20**, 4128–4140 (2020)

35. Vallejo-Melgarejo, L.D., Reifenberger, R.G., Newell, B.A., Narváez-Tovar, C.A., Garcia-Bravo, J.M.: Characterization of 3D-printed lenses and diffraction gratings made by DLP additive manufacturing. Rapid Prototyp. J. **25**, 1684–1694 (2019)

36. O'Neill, P.F., Ben Azouz, A., Vazquez, M., Liu, J., Marczak, S., Slouka, Z., Chang, H.C., Diamond, D., Brabazon, D.: Advances in three-dimensional rapid prototyping of microfluidic devices for biological applications. Biomicrofluidics **8**, 052112 (2014)

37. He, Y., Xue, G.-H., Fu, J.-Z.: Fabrication of low cost soft tissue prostheses with the desktop 3D printer. Sci. Rep. **4**, 1–7 (2014)

38. Guide to Clear 3D Printing.: (2021). https://formlabs.com/blog/3d-printing-transparent-parts-techniques-for-finishing-clear-resin/. Accessed 08 Mar 2021

39. Gross, B.C., Anderson, K.B., Meisel, J.E., McNitt, M.I., Spence, D.M.: Polymer coatings in 3D-printed fluidic device channels for improved cellular adherence prior to electrical lysis. Anal. Chem. **87**, 6335–6341 (2015)

40. Sirjani, E., Migas, M., Cragg, P.J., Dymond, M.K.: 3D printed UV/VIS detection systems constructed from transparent filaments and immobilised enzymes. Addit. Manuf. **33**, 101094 (2020)

41. Tang, C., Vaze, A., Rusling, J.: Automated 3D-printed unibody immunoarray for chemiluminescence detection of cancer biomarker proteins. Lab Chip **17**, 484–489 (2017)

42. Song, M.S., Choi, H.Y., Seong, J.H., Kim, E.S.: Matching-index-of-refraction of transparent 3D printing models for flow visualization. Nucl. Eng. Des. **284**, 185–191 (2015)

43. Wolfe, D., Goossen, K.: Smart Materials and Nondestructive Evaluation for Energy Systems IV, vol. 10601, p. 1060102. International Society for Optics and Photonics (2018)

44. Lee, Y.-S., Bhattacharjee, N., Folch, A.: 3D-printed Quake-style microvalves and micropumps. Lab Chip **18**, 1207–1214 (2018)

45. Scott, C., Potsaid, B., Wen, J.T.: Wide field scanning telescope using MEMS deformable mirrors. Int. J. Optomechatron. **4**, 285–305 (2010)

46. Kheireddine, S., Perumal, A.S., Smith, Z.J., Nicolau, D.V., Wachsmann-Hogiu, S.: Dual-phone illumination-imaging system for high resolution and large field of view multi-modal microscopy. Lab Chip **19**, 825–836 (2019)

47. Salafi, T., Zeming, K.K., Lim, J.W., Raman, R., Seah, A.W.R., Tan, M.P., Zhang, Y.: Portable smartphone-based platform for real-time particle detection in microfluidics. Adv. Mater. Technol. **4**, 1800359 (2019)

48. Jagannadh, V.K., Murthy, R.S., Srinivasan, R., Gorthi, S.S.: Automated quantitative cytological analysis using portable microfluidic microscopy. J. Biophotonics **9**, 586–595 (2016)

49. Yuan, C., Kowsari, K., Panjwani, S., Chen, Z., Wang, D., Zhang, B., Ng, C.J.-X., Alvarado, P.V.Y., Ge, Q.: Ultrafast three-dimensional printing of optically smooth microlens arrays by oscillation-assisted digital light processing. ACS Appl. Mater. Interfaces **11**, 40662–40668 (2019)

50. Kim, Y.T., Bohjanen, S., Bhattacharjee, N., Folch, A.: Partitioning of hydrogels in 3D-printed microchannels. Lab Chip **19**, 3086–3093 (2019)

51. Li, Z., Dey, P., Kim, S.-J.: Microfluidic single valve oscillator for blood plasma filtration. Sens. Actuators B Chem. **296**, 126692 (2019)

52. Ching, T., Toh, Y.-C., Hashimoto, M.: Fabrication of complex 3D fluidic networks via modularized stereolithography. Adv. Eng. Mater. **22**, 1901109 (2020)

53. Park, J., Lee, K.G., Han, D.H., Lee, J.-S., Lee, S.J., Park, J.-K.: Pushbutton-activated microfluidic dropenser for droplet digital PCR. Biosens. Bioelectron. **181**, 113159 (2021)

54. Ong, L.J.Y., Ching, T., Chong, L.H., Arora, S., Li, H., Hashimoto, M., DasGupta, R., Yuen, P.K., Toh, Y.-C.: Self-aligning Tetris-Like (TILE) modular microfluidic platform for mimicking multi-organ interactions. Lab Chip **19**, 2178–2191 (2019)

55. Asiga.: Composer 1.2 Handbook. Asiga, Alexandria (2018)

56. Skliutas, E., Kasetaite, S., Jonušauskas, L., Ostrauskaite, J., Malinauskas, M.: Photosensitive naturally derived resins toward optical 3-D printing. Opt. Eng. **57**, 041412 (2018)

57. Gong, H., Beauchamp, M., Perry, S., Woolley, A.T., Nordin, G.P.: Optical approach to resin formulation for 3D printed microfluidics. RSC Adv. **5**, 106621–106632 (2015)

58. Gojzewski, H., Guo, Z., Grzelachowska, W., Ridwan, M., Hempenius, M., Grijpma, D., Vancso, G.: Layer-by-layer printing of photopolymers in 3D: How weak is the interface? ACS Appl. Mater. Interfaces **12**, 8908–8914 (2020)

59. Vandenberghe, L., Boyd, S.: Convex Optimization. Cambridge University Press, Cambridge (2004)

60. Bertana, V., De Pasquale, G., Ferrero, S., Scaltrito, L., Catania, F., Nicosia, C., Marasso, S.L., Cocuzza, M., Perrucci, F.: 3D printing with the commercial UV-curable standard blend resin: optimized process parameters towards the fabrication of tiny functional parts. Polymers **11**, 292 (2019)

61. Griffiths, C., Howarth, J., De Almeida-Rowbotham, G., Rees, A., Kerton, R.: A design of experiments approach for the optimisation

of energy and waste during the production of parts manufactured by 3D printing. J. Clean. Prod. **139**, 74–85 (2016)

62. Cafieri, S., Monies, F., Mongeau, M., Bes, C.: Plunge milling time optimization via mixed-integer nonlinear programming. Comput. Ind. Eng. **98**, 434–445 (2016)

63. Goh, G.D., Sing, S.L., Yeong, W.Y.: A review on machine learning in 3D printing: applications, potential, and challenges. Artif. Intell. Rev. **54**, 63–94 (2021)

64. Menon, A., Póczos, B., Feinberg, A.W., Washburn, N.R.: Optimization of silicone 3D printing with hierarchical machine learning. 3D Print. Addit. Manuf. **6**, 181–189 (2019)

65. Fraser, L.A., Kinghorn, A.B., Dirkzwager, R.M., Liang, S., Cheung, Y.-W., Lim, B., Shiu, S.C.-C., Tang, M.S., Andrew, D., Manitta, J.: A portable microfluidic aptamer-tethered enzyme capture (APTEC) biosensor for malaria diagnosis. Biosens. Bioelectron. **100**, 591–596 (2018)

66. Brunet, A.R., Labelle, F., Wong, P., Gervais, T.: Reconfigurable microfluidic magnetic valve arrays: towards a radiotherapy-compatible spheroid culture platform for the combinatorial screening of cancer therapies. Sensors **17**, 2271 (2017)

67. Moussus, M., Meier, M.: A 3D-printed Arabidopsis thaliana root imaging platform. Lab Chip **21**, 2557–2564 (2021)

68. Riahi, M.: Fabrication of corner cube array retro-reflective structure with DLP-based 3D printing technology. Opt. Rev. **23**, 442–447 (2016)

69. Arnold, C., Monsees, D., Hey, J., Schweyen, R.: Surface quality of 3D-printed models as a function of various printing parameters. Materials **12**, 1970 (2019)

70. Shallan, A.I., Smejkal, P., Corban, M., Guijt, R.M., Breadmore, M.C.: Cost-effective three-dimensional printing of visibly transparent microchips within minutes. Anal. Chem. **86**, 3124–3130 (2014)

71. Kotz, F., Risch, P., Helmer, D., Rapp, B.E.: Highly fluorinated methacrylates for optical 3D printing of microfluidic devices. Micromachines **9**, 115 (2018)

72. Ross, S.T., Allen, J.R., Davidson, M.W.: Chapter 2—practical considerations of objective lenses for application in cell biology. In: Waters, J.C., Wittman, T. (eds.) Methods in Cell Biology, vol. 123, pp. 19–34. Academic Press, Cambridge (2014)

73. Brennen, C.E.: Cavitation and Bubble Dynamics. Cambridge University Press, Cambridge (2014)

74. Jeon, H., Mirgissa, K.A., Baek, S., Rhee, K., Kim, D.: Excitation-frequency determination based on electromechanical impedance spectroscopy for a laser-microfabricated cavitation microstreaming micromixer. Sens. Actuators A Phys. **326**, 112730 (2021)

75. Hashmi, A., Yu, G., Reilly-Collette, M., Heiman, G., Xu, J.: Oscillating bubbles: a versatile tool for lab on a chip applications. Lab Chip **12**, 4216–4227 (2012)

76. Wiklund, M., Green, R., Ohlin, M.: Acoustofluidics 14: Applications of acoustic streaming in microfluidic devices. Lab Chip **12**, 2438–2451 (2012)

77. Kaba, A.M., Jeon, H., Park, A., Yi, K., Baek, S., Park, A., Kim, D.: Cavitation-microstreaming-based lysis and DNA extraction using a laser-machined polycarbonate microfluidic chip. Sens. Actuators B Chem. **346**, 130511 (2021)

78. Okabe, Y., Chen, Y., Purohit, R., Corn, R.M., Lee, A.P.: Piezoelectrically driven vertical cavity acoustic transducers for the convective transport and rapid detection of DNA and protein binding to DNA microarrays with SPR imaging—a parametric study. Biosens. Bioelectron. **35**, 37–43 (2012)

79. Liu, R.H., Yang, J., Pindera, M.Z., Athavale, M., Grodzinski, P.: Bubble-induced acoustic micromixing. Lab Chip **2**, 151–157 (2002)

80. De Vellis, A., Gritsenko, D., Lin, Y., Wu, Z., Zhang, X., Pan, Y., Xue, W., Xu, J.: Drastic sensing enhancement using acoustic bubbles for surface-based microfluidic sensors. Sens. Actuators B Chem. **243**, 298–302 (2017)

81. Conde, A.J., Keraite, I., Ongaro, A.E., Kersaudy-Kerhoas, M.: Versatile hybrid acoustic micromixer with demonstration of circulating cell-free DNA extraction from sub-ml plasma samples. Lab Chip **20**, 741–748 (2020)

82. Zhang, J., Xiao, P.: 3D printing of photopolymers. Polym. Chem. **9**, 1530–1540 (2018)

83. Carve, M., Wlodkowic, D.: 3D-printed chips: Compatibility of additive manufacturing photopolymeric substrata with biological applications. Micromachines **9**, 91 (2018)

84. Lee, J.-Y., An, J., Chua, C.K.: Fundamentals and applications of 3D printing for novel materials. Appl. Mater. Today **7**, 120–133 (2017)

85. ASIGA.: Safety data sheet PlasCLEAR v2. Asiga, Alexandria (2017)

86. Zhu, F., Skommer, J., Macdonald, N.P., Friedrich, T., Kaslin, J., Wlodkowic, D.: Three-dimensional printed millifluidic devices for zebrafish embryo tests. Biomicrofluidics **9**, 046502 (2015)

87. Piironen, K., Haapala, M., Talman, V., Järvinen, P., Sikanen, T.: Cell adhesion and proliferation on common 3D printing materials used in stereolithography of microfluidic devices. Lab Chip **20**, 2372–2382 (2020)

88. Choi, J.W., Wicker, R.B., Cho, S.H., Ha, C.S., Lee, S.H.: Cure depth control for complex 3D microstructure fabrication in dynamic mask projection microstereolithography. Rapid Prototyp. J. **15**, 59–70 (2009)

89. Zhang, Y.F., Ng, C.J.X., Chen, Z., Zhang, W., Panjwani, S., Kowsari, K., Yang, H.Y., Ge, Q.: Miniature pneumatic actuators for soft robots by high-resolution multimaterial 3D printing. Adv. Mater. Technol. **4**, 1900427 (2019)

90. Abramowitz, M., Spring, K.R., Keller, H.E., Davidson, M.W.: Basic principles of microscope objectives. Biotechniques **33**, 772–781 (2002)

91. Ahmed, D., Mao, X., Shi, J., Juluri, B.K., Huang, T.J.: A millisecond micromixer via single-bubble-based acoustic streaming. Lab Chip **9**, 2738–2741 (2009)

92. Rasouli, M.R., Tabrizian, M.: An ultra-rapid acoustic micromixer for synthesis of organic nanoparticles. Lab Chip **19**, 3316–3325 (2019)

93. Liu, R.H., Yang, J., Lenigk, R., Bonanno, J., Grodzinski, P.: Self-contained, fully integrated biochip for sample preparation, polymerase chain reaction amplification, and DNA microarray detection. Anal. Chem. **76**, 1824–1831 (2004)

94. Palenzuela, C.L.M., Pumera, M.: (Bio) Analytical chemistry enabled by 3D printing: sensors and biosensors. Trends Anal. Chem. **103**, 110–118 (2018)